

A SUZAKU X-RAY STUDY OF THE PARTICLE ACCELERATION PROCESSES IN THE RELATIVISTIC JET OF BLAZAR MRK 421

ALFRED B. GARSON III
 Washington University in St. Louis
 and The McDonnell Center for the Space Sciences, St. Louis, MO 63130
agarson3@hbar.wustl.edu

MATTHEW G. BARING
 Department of Physics and Astronomy MS-108,
 Rice University, P.O. Box 1892, Houston, TX 77251, U.S.A.
baring@rice.edu

AND

HENRIC KRAWCZYNSKI
 Washington University in St. Louis
 and The McDonnell Center for the Space Sciences, St. Louis, MO 63130
krawcz@wuphys.wustl.edu

Accepted for publication in The Astrophysical Journal

ABSTRACT

We report on the findings of a 364 ksec observation of the BL LAC object Mrk 421 with the X-ray observatory Suzaku. The analysis in this paper uses fluxes and hardness ratios in the broad energy range from 0.5 keV to 30 keV. During the course of the observation, the 0.5 keV - 30 keV flux decreased by a factor of ~ 2 and was accompanied by several large flares occurring on timescales of a few hours. We find that fitting a broken power model to spectra from isolated epochs during the observation describes the data well. Different flares exhibit different spectral and hardness ratio evolutions. The cumulative observational evidence indicates that the particle acceleration mechanism in the Mrk 421 jet produces electron energy distributions with a modest range of spectral indices and maximum energies. We argue that the short-timescale X-ray spectral variability in the flares can be attributed *mostly* to intrinsic changes in the acceleration process, dominating other influences such as fluctuations in the Doppler beaming factor, or radiative cooling in or outside the acceleration zone.

Subject headings: BL Lac, blazars, jets, X-ray: general — blazars, jets, X-ray: individual (Mrk 421)

1. INTRODUCTION

TeV blazars exhibit νF_ν spectral energy distributions (SEDs) with two broad peaks: one in soft to medium X-rays and one at GeV energies. The amplitude and the position of the peak changes with time, sometimes in a correlated way (e.g. Blazewski et al. 2005). The emission is highly polarized in radio through optical wavelengths (e.g. Piner & Edwards 2005, Homan et al. 2000, Lister & Smith 2000). The radio through X-ray spectrum is thought to be the result of synchrotron emission from the highest energy electrons and positrons accelerated to Lorentz values $\gamma_e \gg 10^2$ by shock fronts in the jet. Inverse Compton scattering from the same population of electrons and their synchrotron photons may be responsible for the peak at higher energies. This synchrotron self-Compton (SSC) model is contrasted by external Compton (EC) models. In the latter the low-energy photons originate outside the emission volume of the gamma-rays. Possible sources of target photons include: accretion disk photons radiated directly into the jet, accretion disk photons scattered by emission-line clouds or dust in the jet, synchrotron radiation re-scattered back into the jet by broad-line emission clouds, jet emission from an outer slow jet sheet, or emission from faster or slower portions of the jet (Ghisellini & Maraschi 1989, Macomb et al. 1995, Mastichiadis & Kirk 1997, Ghisellini et al. 2005, Georganopoulos et al. 2004). There are also hadronic models for the TeV emission. An example for a hadronic γ -ray production mechanism is pion

photoproduction from either low energy synchrotron photons or photons external to the jet (e.g. Mannheim 1993, Mücke et al. 2003). Synchrotron emission from protons in compact regions of the jet is another explanation (Aharonian 2000).

Blazars are known for their variability at X-ray and γ -ray energies. The X-ray and γ -ray fluxes can vary rapidly and are often correlated, with a notable exception of orphan TeV flares (e.g. Krawczynski et al. 2004). X-ray flaring epochs lasting many months have been observed as well as sub-hour flares (e.g. Cui 2004). The source of flaring activity has been attributed to internal shocks within the jet (Rees 1978, Spada et al. 2001), ejection of relativistic plasma into the jet (Böttcher et al. 1997, Mastichiadis & Kirk 1997), as well as reconnection events in a magnetically dominated jet (Lyutikov 2003, Giannios et al. 2009).

Constraining blazar jet models generally requires simultaneous observations across the radio to gamma-ray spectrum. However, these probes can be augmented by focusing on the nuances in a particular waveband. Such is the approach here, specifically with X-rays and their variable signals, since the high count rates and good spectral resolution in this band provide powerful additional probes of the jet environment. Note that using the X-ray spectra of TeV blazars can provide constraints on the modeling of the overall SED. The position of the synchrotron peak has become a marker for classes of BL Lac objects (Padovani & Giommi 1995). LBL (Low energy peaked BL Lac) and HBL (high energy peaked BL Lac) designate

whether the synchrotron peak in is the IR-optical or UV-X-ray bands, respectively. Monitoring spectral parameters as flaring events evolve gives insight into the mechanics of the emission (Kirk et al. 1998). From their analysis, for simple models involving a single electron population, different hardness ratio (HR) trends will be observed for varying fluxes depending on the timescales of the processes involved. In the HR-flux plane, there will be clockwise movement as time progresses if the high energy component varies faster than the low energy component, where electron cooling times exceed the acceleration time; this case is more probably sampled below the X-ray band. Counter-clockwise motion in the HR-flux plane is predicted if the observation is made near the synchrotron cutoff frequency, specifically when the cooling and acceleration timescales are roughly equal.

In the case of TeV bright blazars like Mrk 421, individual sources have shown both hard and soft lags (e.g. Kataoka et al. 2000, Takahashi et al. 2000, Sato et al. 2008). Such lags are apparent when a light curve is examined in two energy bands (canonically separated at 2 keV). Trends in the count rate do not always occur simultaneously in both energy windows. Features can also be observed first at high energies (soft lag) or first at low energies (hard lag).

The peak energy and curvature of the X-ray spectrum have been shown to be anti-correlated for different acceleration scenarios such as stochastic or energy dependent acceleration (e.g. Kardeshev 1962, Massaro et al. 2004, Stawarz & Petrosian 2008). X-ray measurements also can provide limits on physical properties of the emitting region such as its size (e.g. $R \approx 10^{14}$ cm; see Tramacere et al. 2009). Thus, although multi-wavelength observations are crucial for investigating acceleration and emission processes, careful study of X-ray observations from TeV blazars can give insight into the mechanisms responsible for the populations of charged particles and photons in the jet.

Mrk 421 is a TeV blazar and, at a redshift of $z=0.031$, it is one of the closest and best-studied BL Lac objects. It was the first extra-galactic TeV source (Punch et al. 1992) and has been the target of many multiwavelength campaigns (e.g. Takahashi et al. 1996, Krawczynski et al. 2001, Rebillot et al. 2006, Gupta, et al. 2008, Fossati et al. 2008). The synchrotron peak in Mrk 421's spectrum ranges from a fraction of a keV to several keV and spectral variability as a function of flux level has been observed (Fossati et al. 2000). In general, the spectrum becomes harder for higher fluxes, both in the X-ray band (e.g. Fossati et al. 2008; Tramacere et al. 2009) and in the gamma-ray regime (Krennrich et al. 2002, Aharonian et al. 2002). It also now has a well-measured GeV-band spectrum from *Fermi*'s Large Area Telescope (see Abdo et al. 2009) that provides useful constraints on the high energy electron population using an inverse Compton signal interpretation. The relationship between the *Fermi* and *Suzaku* spectra will be discussed in Section 4 below.

Takahashi et. al (1996) observed a soft lag (<1.5 keV) in X-rays. When attributed to synchrotron electron lifetimes, the magnetic field strength and electron Lorentz factor were found to be $B \sim 0.2$ G and $\gamma_e \sim 10^6$, respectively. *Swift* observations indicate that each flare has it's own competition between time scales involved with electron acceleration and cooling. The energy spectrum of the electrons associated with the UV-X-ray emission can be described with a curved population (Tramacere et al. 2007, Tramacere et al. 2009). Previous *Suzaku* observations suggest that the emission contains a steady component and a variable component. The latter may

be attributed to localized Fermi I type acceleration in individual shocks, while the former may be due to superposition of shocks at larger distances from the jet or other processes (Ushio et al. 2009).

In this paper, we give the findings from a 4-day observation of Mrk 421 with the X-ray satellite telescope *Suzaku* in May 2008. This pre-dates the launch of *Fermi*. Simultaneous XMM-Newton and VERITAS gamma-ray observations in a separate campaign were described by Acciari et al. (2009). Another paper combines a large number of multiwavelength observations of Mrk 421, including the XMM Newton, *Suzaku* and VERITAS data (Acciari et al. 2010).

We investigate the evolution of spectral parameters over the duration of the observation. The study presented in this paper benefits from the long exposure of 364 ksec and the excellent sensitivity of *Suzaku* over the 0.5 keV to 30 keV energy range. Compared to the 2006 *Suzaku* observation campaign presented by Ushio et al. (2009), the observations presented here reveal the source in a lower flux state. In Section 2 we describe the *Suzaku* instruments, give the essentials of this observation, and outline the analysis protocol. The results are detailed in Section 3. These are followed in Section 4 by the discussion of the interpretation and implications of the findings, highlighting how the X-ray spectrum and variability impacts our understanding of the Mrk 421 jet environment and the particle acceleration properties therein.

2. OBSERVATIONS AND DATA REDUCTION

Suzaku (Mitsuda et al. 2007) is an X-ray observatory with two primary instruments. The X-ray Imaging Spectrometer (XIS) is an imaging X-ray CCD instrument with 3 operating detectors: two are sensitive from 0.5 keV to 10.0 keV (XIS0 and XIS3), while the backside-illuminated XIS1 extends the low energy range to 0.2 keV (Koyama et al. 2007). Complementary to and co-aligned with the XIS is the Hard X-ray Detector (HXD) which is a well-type instrument composed of GSO scintillator and silicon PIN diodes. The PIN detectors observe in the 12 keV to 60 keV energy band, while the GSO can detect up to gamma-ray energies (Takahashi et al. 2007, Kokubun et al. 2007). This observation (ID 703043010) was triggered from a detection by the ground-based atmospheric Čerenkov telescope, VERITAS. Mrk 421 was observed May 5 2008 02:52 (MJD 54591) through May 9 08:24 (MJD 54595). *Suzaku* has two observation modes which place a source either in the center of the HXD or XIS fields of view (FOV). HXD pointing was selected for this observation. The XIS instruments were operated in 1/8 window mode.

2.1. Data Reduction

The XIS and HXD event files were used for this study. Standard reduction and processing were performed using HEASOFT v6.8 and *Suzaku* ftools v15. The files were cleaned with the selection criteria: cutoff rigidity larger than 6 GV/c, Earth rim elevation angle greater than 5° and 20° during the night and day, respectively.

XIS events were extracted from a source region with an inner radius of 35 pixels and an outer radius of 408 pixels. The extent of the inner radius is such that pile-up effects were minimized for the selected events. The background was selected from an annulus outside of the source region, with inner and outer radii of 432 pixels and 464 pixels, respectively. The response matrix and effective area were calculated for each XIS sensor using the *Suzaku* ftools tasks, *xisrmfgen* and *xissimarfr*.

gen (Ishisaki et al. 2007). XIS1 data were not included in this analysis; including the XIS1 spectra did not improve the quality of the fits. As the XIS0 and XIS3 have similar responses, their data were summed.

PIN data were extracted from the HXD uncleaned event files after standard screening. The tuned background model supplied by the *Suzaku* team was used for Non X-ray Background (NXB) events. The source spectra were corrected for deadtime using *hxdtdcor*. The PIN light curves were deadtime-corrected bin-by-bin (after incorporating 4 ksec - 6 ksec bins) using pseudo events generated in orbit. The background and spectra light curves were corrected for their 10x oversampling rate. We estimate the cosmic X-ray background (CXB) contribution to the PIN background using the model given in Gruber et al. (1999), which is folded with the PIN response to estimate the CXB rate.

3. TEMPORAL AND SPECTRAL RESULTS

3.1. Light Curves

We plot the time history of the observation in Figure 1. Light curves are given in 2 energy bands for each instrument: 0.5 keV - 2.0 keV and 2.0 keV - 10.0 keV for the XIS; 10.0 keV - 20 keV and 20 keV - 30 keV for the PIN. The three lowest energy bands include similar count rate evolution throughout the observation, while the highest energy band does not have significant changes. Overall, the rates decrease by up to a factor of 2 over the course of the observation. Rates decrease from ~ 50 cts/sec to ~ 20 cts/sec in the 0.5 keV - 2 keV range and 0.16 cts/sec to 0.13 cts/sec in the 20 keV - 30 keV band. The general decline in rates is marked by several shorter duration flares occurring at 80ks, 120ks, 140ks, 260ks, 310ks and 340ks after the start of the observation.

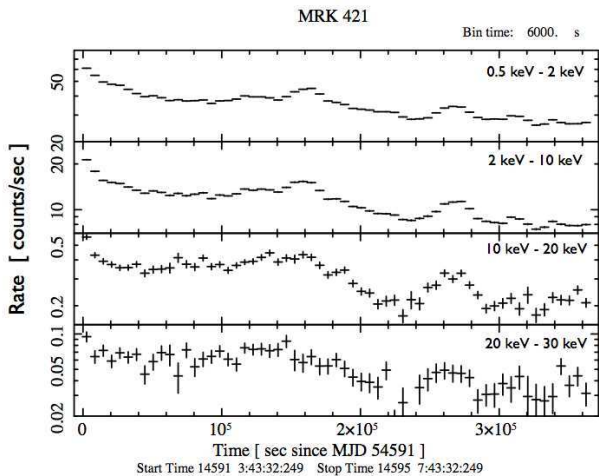


FIG. 1.— These light curves illustrate the rates measured by the XIS and PIN detectors. Curves are given for (top to bottom) 0.5 keV - 2 keV, 2 keV - 10 keV, 10 keV - 20 keV, and 20 keV - 30 keV. Over the course of the observation, the rates decrease by a factor of ~ 2 . The light curve is marked with 2 strong flares and several small flares.

The light curves begin with a rapid decline in rates for the initial 20ks of the observation. There is a general leveling off with some small variations in rates over the next 100ks. A strong ~ 25 ks flare is then seen which brings rates close to their original level. This flare is shorter in duration for higher energy bands. The rates then smoothly decline for ~ 30 ks. During this time, a flare is observed in the 12 keV - 20 keV band, but not in any other bands. There is then a second large flare which is seen in the three lower energy ranges. The last 50ks of the

observation has two small flares spanning the period.

We investigate the time evolution of the hardness ratio (HR) of the XIS events. It is convenient to divide the observational window into two bands, 0.5 - 2 keV (*a*) and 2 - 10 keV (*b*), and define the HR as either the ratio of counts (b/a), or the ratio of the difference and sum of counts ($(b-a)/(b+a)$), a standard protocol. Here we use the former definition of HR. This differs slightly from the approach of Tramacere et al. (2009), who use the spectral index at 1 keV to prescribe a hardness ratio.

Figure 2 shows the 0.5 keV - 2.0 keV (*top*) and 2 keV - 10 keV (*middle*) rates, and the corresponding hardness ratio (*bottom*). At the start of the observation, the rates decline quickly as does the HR. At a time of ~ 20 ks, the HR begins to increase while the rates in both bands continue to decrease then stabilize for a duration of ~ 8000 sec. For the remainder of the observation, the HR follows the flux. It becomes harder for larger fluxes so that the HR vs time plot largely reproduces the features in the light curves. Using the XIS response and *xspec*, we simulate spectra for a simple power-law model using photon indices between 2.2 and 2.5. We calculate the hardness ratio measured by XIS for these simulated observations and indicate the corresponding position in the lower panel of Figure 2 (*horizontal dotted lines*) for comparison with the measured HRs.

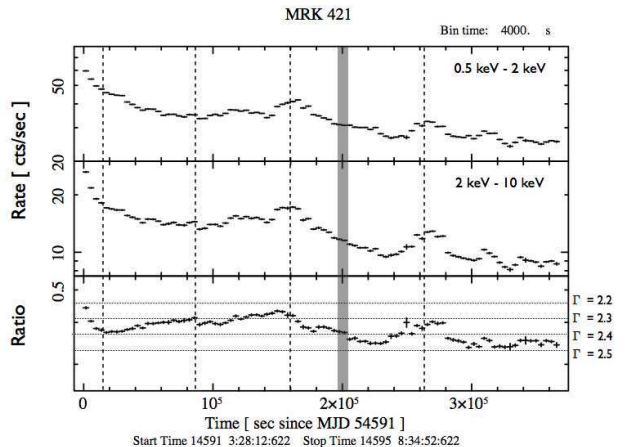


FIG. 2.— This light curve samples the XIS count rate with slightly finer binning (4000s) than in Figure 1 (6000s). The high and low energy bands are given in the top and middle panels, respectively. The bottom panel shows the corresponding hardness ratio ($HR = \text{rate}_{\text{High}}/\text{rate}_{\text{Low}}$). Using the XIS response files, pure power-law spectra observations were simulated. The horizontal dotted lines in the lower panel give expected hardness ratios using simulated power-law spectra with a range of power-law photon indices. The shaded region near 2×10^5 sec indicates the coincident VERITAS observation window from Acciari et al. (2009).

The vertical lines in Figure 2 are to aid the eye in comparing trends between the rates in the two energy bands and the HR. The first vertical line indicates when the HR changes from decreasing to increasing trend while the count rates continue to decrease. The second vertical line shows a time when the rates and the HR level off and drop during a small flare. The third vertical line marks the peak of a large flare (*Flare 1*) in both energy bands. However it is obvious that the HR peaked ~ 20 ksec prior to the peak in rates. The last vertical line is again placed at a peak (*Flare 2*) in the count rates. For this flare, the HR peak is located closer in time to the peak rate, however the subsequent decrease in the HR is delayed compared to the rate decrease. The shaded gray region in Figure 2 denotes the observation window for the VERITAS campaign described in Acciari et al. 2009; see also Acciari et al. 2010).

3.2. Spectra

During fitting, events with deposited energy between 1.5 keV and 2.5 keV were excluded from the XIS data set due to uncertainties in the instrument response (Ushio et al. 2009). Events with energy between 10 keV and 25 keV were included from PIN data. The resulting spectrum was fit with a galactic absorption \times broken powerlaw. The galactic absorption parameter, n_H , was kept constant at the value of $1.61 \times 10^{20} \text{ cm}^{-2}$ acquired from the CIAO tool Colden¹. Once the normalization parameter was fit for the model, it was frozen while the low energy photon index (Γ_1), break energy (E_{br}), and high energy photon index (Γ_2) were fit independently. Finally, all parameters were simultaneously fit. Note that while similarly good spectral fits were produced using power-law with exponential cutoff models for a few of the results presented here, broken power-law fits were superior to other spectral functions for the majority of time intervals. For broken power-law fits, the average reduced χ^2 is 1.1 for 41 degrees of freedom (dof) with a standard deviation of 0.34, while power-law with exponential cutoff fits produced average reduced χ^2 of 4.05 for 42 dof with a standard deviation of 2.1.

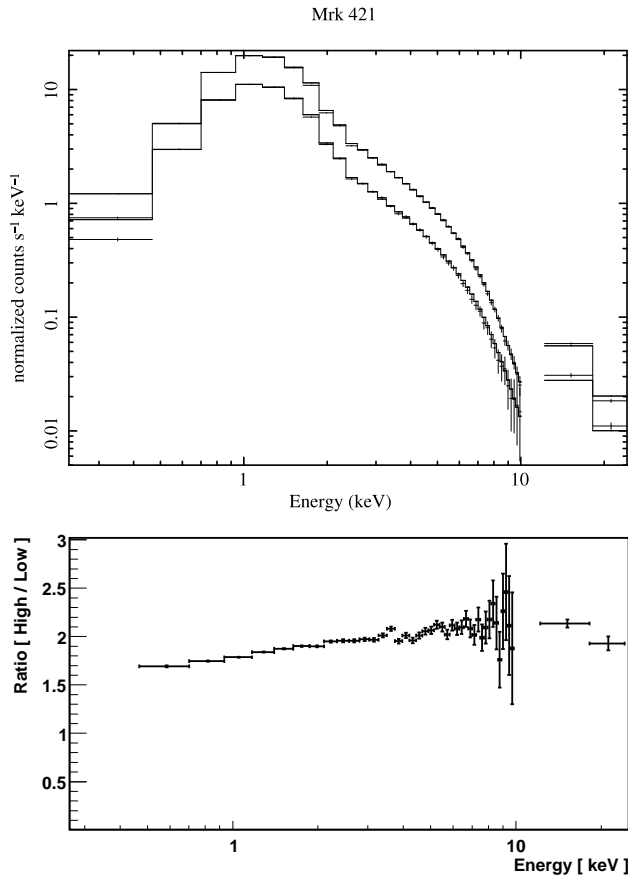


FIG. 3.— The XIS and PIN observed spectra are given for the first ~ 20 ks (*High*) and the final ~ 20 ks (*Low*) of the observation (*top panel*). The bottom panel plots the ratio, $\text{Rate}_{\text{High}}/\text{Rate}_{\text{Low}}$, as a function of energy. A factor of ~ 2 count rate decrease can be seen at most energies between 3 keV and 20 keV while smaller ratios occur at lower energies.

Comparing the spectra at the endpoints of the observation can give insight into the overall evolution of the emission as a function of energy. The upper panel of Figure 3 plots the XIS and PIN spectra for the first as well as final ~ 20 ks of the observa-

tion. The best fit broken power-law models are also shown. The best fit parameters for the start of the observation are $\Gamma_1 = 2.31 \pm 0.007$, $\Gamma_2 = 2.6 \pm 0.008$, $E_B = 2.8 \pm 0.075$ keV, and normalization of $0.37 \pm 0.0006 \text{ cts s}^{-1} \text{ keV}^{-1}$ producing a reduced χ^2 of 1.774. The best fit parameters for the end of the observation are $\Gamma_1 = 2.39 \pm 0.03$, $\Gamma_2 = 2.62 \pm 0.01$, $E_B = 2.37 \pm 0.3$ keV, and normalization of $0.2 \pm 0.0008 \text{ cts s}^{-1} \text{ keV}^{-1}$ producing a reduced χ^2 of 1.19. It is apparent that the rates do decline over the course of the observation. The lower panel shows the hardness ratio, $(\text{Rate}_{\text{High}} / \text{Rate}_{\text{Low}})$, highlighting beginning and end intervals of the 364 ksec observation. The largest values for the ratio occur at $\sim 8 \text{ keV} - \sim 10 \text{ keV}$, indicating an overall slight softening trend. Observe that these spectra are generally considerably steeper than those for the intense flare activity reported for 2006 *Swift* observations of Mrk 421 in Tramacere et al. (2009).

In addition to analyzing spectra at the onset and end of the observation, we construct 12 smaller time bins describing the entire observation and fit the corresponding XIS and PIN spectra with a broken power-law model. The chance probability associated with the reduced χ^2 -values of the fits have values between 0.01 and 0.96, indicating satisfactory fits. The best fit parameters are given as a function of time in Figure 4. It is not possible to fit the time averaged spectrum satisfactorily with a power-law, power-law with high energy cutoff, or broken power-law models. This is not unreasonable due to the wide range of flux and spectral variability observed in the shorter time intervals.

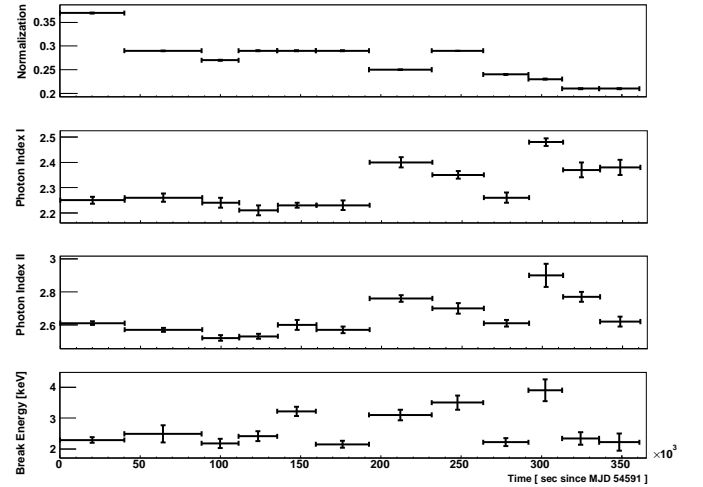


FIG. 4.— This figure plots the best fit parameters and 1σ confidence ranges for different times during the observation using a broken power-law model. The panels (*top-to-bottom*) give the evolution of the flux normalization [photons $\text{sec}^{-1} \text{ keV}^{-1}$], Γ_1 , Γ_2 , E_B [keV].

Figure 5 investigates the correlations between flux normalization, Γ_1 , Γ_2 , and E_{br} for the 12 time intervals in Figure 4. The upper left panel shows that Γ_1 increases somewhat for larger E_{br} values, which is also the case for Γ_2 and E_{br} (*lower left panel*); the scatter in these trends is large. The upper right panel shows no correlation between E_{br} and the normalization. Finally, the lower right panel demonstrates that the two photon indices increase and decrease together, as would be expected with slight variations in the maximum energy of the radiating particles. Insights gleaned from these correlation plots are discussed in Section 4.

¹<http://cxc.harvard.edu/toolkit/colden.jsp>

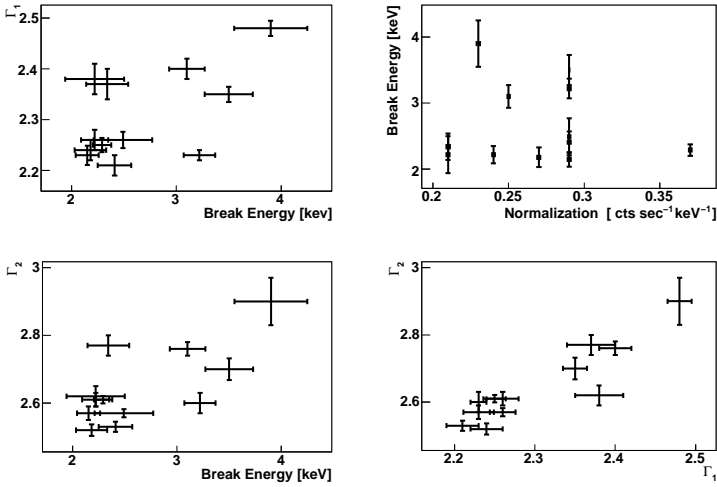


FIG. 5.— Best fit parameters from the four panels of Figure 4 are plotted against each other. The upper left figure plots the correlation of E_{br} and Γ_1 . The lower left panel shows the relationship between E_{br} and Γ_2 . The upper right panel gives E_{br} vs. flux normalization which shows no correlation. The lower right panel shows the relationship between Γ_1 and Γ_2 . The two photon indices increase and decrease together.

Further understanding can be provided by exploring hardness ratio (HR) variations during flares. In Figure 6, HR-flux diagrams are given for the two most prominent flares (1.5×10^5 sec and 2.5×10^5 sec Fig 1). The left panels show the light curves in two energy bands from XIS observations. The higher energy rates have been multiplied by a factor of 3 for clarity. We see that for the *Flare 1* (top panels), there is initial clockwise motion which quickly changes to a larger counter-clockwise arc through the HR-flux plane. *Flare 2* also shows both clockwise and counter-clockwise motion but in a smaller figure-8 pattern. These characteristics of spectral hysteresis are similar to a subset of the *Swift* data reported in Tramacere et al. (2009) for 2006 observations of Mrk 421 flares. The HR-flux trend of an observation can be an indicator of relative time scales for processes involved with acceleration and emission (see Kirk, Rieger & Mastichiadis 1996; Tramacere et al. 2009 and references therein for a discussion). For clockwise motion, the cooling time will be longer than the acceleration time. The two timescales are comparable for counter-clockwise trends.

4. SPECTRAL INTERPRETATION AND DISCUSSION

One of the key results from this observation campaign is that we observe different spectral evolution for similar flares. The different spectral evolutions during different flares exclude models in which flux and spectral variations are caused exclusively by variations of the Doppler beaming factor. Furthermore, they do not concur with simple models where particles are always accelerated with the same spectral index and cool radiatively. Therefore, we conclude there have to be intrinsic variations of the spectral index and density of the radiating (electron) population. To be more precise, such particles are injected with a power-law $dN_e/d\gamma_e \propto n_e \gamma_e^{-\sigma}$, and both n_e and σ vary from flare to flare and also during a flare. This conclusion is underpinned by our reported *Suzaku* detection of rapid flux and index variations in the somewhat steep X-ray spectra.

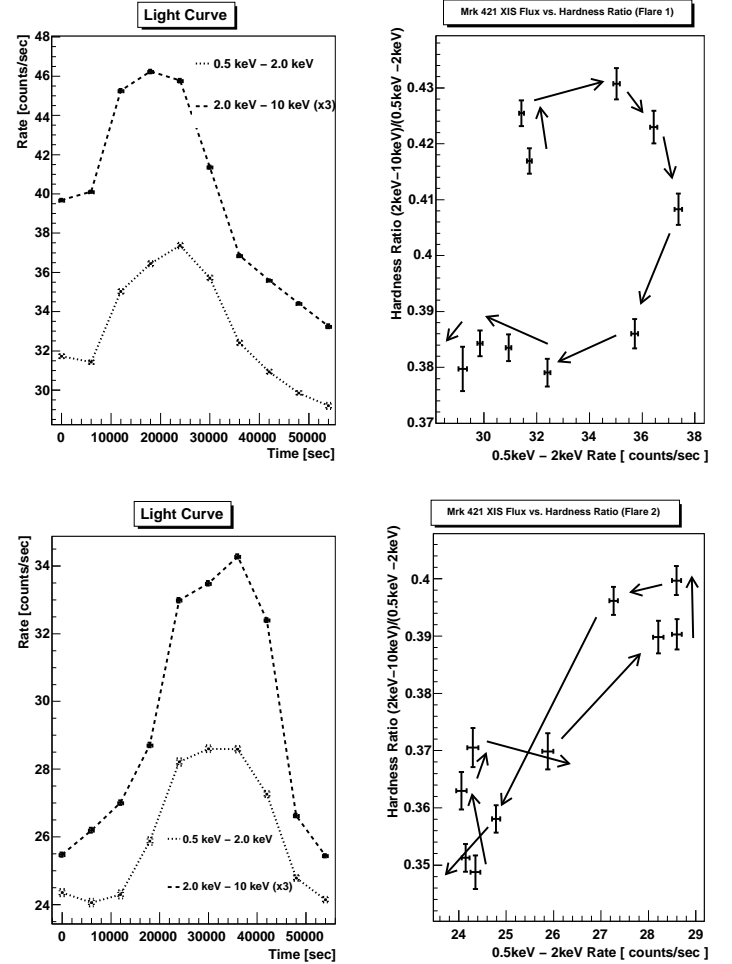


FIG. 6.— The flux vs. hardness ratio plots of two well-defined flares show different motions in the HR-flux plane. The left panels show the XIS light curves for the flares in two energy bands: 0.5 keV - 2 keV ($Rate_{high}$: dotted line) and 2 keV - 10 keV ($Rate_{low}$: dashed line). The rates in the higher energy band have been multiplied by 3 for clarity. The right panels plot the hardness ratio ($Rate_{high}/Rate_{low}$) vs $Rate_{low}$ correlation for these flares. For *Flare 1* (upper right), there is initially a clockwise trend followed by larger counter-clockwise movement. The lower right panel also shows a shift from clockwise to counter-clockwise but in a figure 8 pattern. Here, *Flare 1* (top panels) occurs at $\sim 1.5 \times 10^5$ sec into the observation and *Flare 2* (bottom panels) occurs at $\sim 2.5 \times 10^5$ sec.

In the following interpretative discussion, two scenarios will be addressed in turn, after the issue of Doppler boosting variations is first touched upon. First, the case that radiative cooling does not lead to a steepening of the observed X-ray energy spectra is considered. Subsequently, we turn to the scenario of efficient radiative cooling that spawns a steepening of the observed spectral indices by $\delta\Gamma = 1/2$. We remark that several VERITAS TeV gamma-ray observations were taken during our *Suzaku* observations (see Acciari et al. 2009; Acciari et al. 2010). These observations revealed modest TeV gamma-ray flares, demonstrating that the synchrotron spectral power dominated the inverse Compton emissive power, which is also the situation for much earlier Whipple-era observations (e.g. see the broadband data depiction in Inoue & Takahara 1996). The following discussion can thus safely neglect complications arising from inverse Compton cooling in the Klein-Nishina regime, which in other circumstances can modify the distribution of the highest energy particles, and therefore also the shape of the X-ray synchrotron continuum.

To provide context for the results of this paper in the light of other multifrequency observations, we note that it is likely that the radio emission observed from Mrk421 does not come from precisely the same spatial region as the X-ray emission. For BL Lac type objects, no convincing radio/x-ray correlation has ever been established. For leptonic models that explain the observed X-ray emission without giving a measurable radio flux, see Rebillot et al. (2003) and Krawczynski et al. (2001). The discussion here therefore focuses on explaining the high energy emission from electrons close to the high energy cutoff of the electron energy spectrum. While multiwavelength SED modeling of blazars with radio-to-X-ray synchrotron and gamma-ray inverse Compton signals typically constrains the approximate maximum Lorentz factor of the electrons, the mean magnetic field strength and the bulk Doppler factor δ of the jet (e.g. see Bednarek & Protheroe 1997; Mastichiadis & Kirk 1997), SED fluctuations augment such by probing different jet environmental quantities. This is the focus here, and X-ray observations afford stronger diagnostics than do the GeV and TeV bands due to their high count rates. For example, typical variability in *Fermi*-LAT data on blazars samples timescales of a few days to a week at best (Abdo et al. 2010b) when acquiring sufficient count statistics. TeV gamma-ray energy spectra with spectral index errors < 0.1 can be acquired on short (~ 10 min) time scales - but require extremely strong flares.

To begin the interpretive focus on the X-ray variability, in principal, adjustments of the spectral indices and hardness ratios can be generated by fluctuations in the Doppler beaming factor δ during flares. Such δ variations can arise in bent jets, such as the scenario envisaged for *Fermi*-LAT and other wavelength observations of the quasar 3C 279 (Abdo et al. 2010a). Consider the correlation plots in Figure 5. In the absence of other influences, changes in δ should manifest themselves as a scaling of the break energy $E_{\text{br}} \propto \delta$ (blueshifting) and an associated scaling of the flux at E_{br} as δ^4 . This correlation should hold approximately even if the 0.2-10 keV window samples a portion of a larger SED curvature. It is clearly not seen in the upper right panel of Figure 5, indicating that some other environmental fluctuation is operative. If the SED curvature is broad, one might expect that higher break energies in the fits will correlate with lower Γ_1 . The opposite is suggested in the upper left panel of Figure 5, but the scatter is large, and the E_{br} range is small. In terms of the HR-flux diagrams in Figure 6, pure Doppler factor δ fluctuations should yield a strong correlation between the hardness ratio and the count rate below 2 keV: essentially a diagonal trace from lower left to upper right. This is clearly not seen for *Flare 1*. There is more of an indication for *Flare 2*, but significant deviations from a clean correlation occur when taking into account the evolutionary track. Accordingly, something deeper than just simple Doppler boosting variations must be active in the jet environment, and our attention turns to the particle acceleration properties in shocks within the Mrk 421 jet.

The observed spectral fluctuation signatures are therefore interpreted now in the light of expectations from diffusive shock acceleration theory. This logical step can be taken because the power-law is both well-established below E_{br} and is considerably flatter than the steeper spectra seen in the TeV band that might typify the onset of a cutoff. If the spectral indices $2.2 \lesssim \Gamma_1 \lesssim 2.5$ identified in Figures 5 and 6 are attributed to synchrotron emission from a particle distribution $dN_e/d\gamma_e \propto \gamma_e^{-\sigma}$ (below a maximum Lorentz factor cutoff γ_{max}), then for uncooled synchrotron scenarios, $\Gamma_1 = (\sigma + 1)/2$. These

cases are where the accelerated population is continually replenished in the emission region on timescales inferior to the synchrotron cooling timescale $t_{\text{syn}} = 4\pi m_e c / (\sigma_T B^2) \gamma_e^{-1}$. Observe that $t_{\text{syn}} \sim 1$ hour for $B = 0.1$ G and $\gamma_e \sim 10^7$, parameters that would place the synchrotron turnover at $\sim 150\delta$ keV. In this scenario, the acceleration timescale needs to be comparable to the flare duration or shorter, while t_{syn} needs to exceed the flare timescale, a situation that occurs for lower γ_e that can move the synchrotron turnover down to the *Suzaku* window. For such an uncooled acceleration picture, the X-ray index in any time interval leads to a constraint on the electron index σ , and we find $3.4 \lesssim \sigma \lesssim 4$. The physical conditions in the Mrk 421 jet environment that can generate σ in this range can be assessed using the Monte Carlo simulational modeling of Baring & Summerlin (2009), Baring (2010), and Ellison & Double (2004), of particle acceleration at relativistic shocks. These works provided a useful and expansive complement to earlier semi-analytic investigations of Kirk & Schneider (1987) and Kirk & Heavens (1991) that employed eigenfunction techniques to solve the diffusion-convection equation at mildly-relativistic shocks.

The spectral index parameter space explored in these simulational studies clearly indicated that values of $\sigma > 3$ are appropriate only for so-called *superluminal shocks*, i.e. those where $u_1 / \cos \Theta_{Bn1} > c$. Here u_1 is the component of the upstream flow speed normal to the shock in its rest frame. For the relativistic outflows commonly invoked in blazar jets, one naturally expects $u_1 \sim c$. Also, Θ_{Bn1} is the angle the magnetic field vector makes to the shock normal in the upstream fluid rest frame. Therefore, superluminal (and oblique, $\Theta_{Bn1} > 0^\circ$) conditions in Mrk 421's jet would naturally be expected. However, Baring & Summerlin (2009) also observed that to generate $\sigma > 3$, it would be necessary for the field turbulence in the shock neighborhood to not be too strong, perhaps limiting field fluctuations to $\delta B/B \lesssim 0.1$, so that particle diffusion is not too near the isotropic Bohm limit (essentially occurring for $\delta B/B \sim 1$). This is an interesting environmental constraint that lowers the expected acceleration time t_{acc} (e.g. Jokipii 1987) due to the inefficient trapping of charges in oblique shocks, a property that is directly responsible for steeper power-laws with $\sigma \gtrsim 3$.

Consider instead a strongly-cooled synchrotron emission picture, where the shock injects relativistic particles into a larger region where the synchrotron cooling timescale exceeds the injection timescale. Invoking such to explain the *Suzaku* power-law indices, one infers $\sigma = 2(\Gamma_1 - 1)$ for the shock acceleration spectral index, since synchrotron cooling steepens the electron power-law by an index of unity; the index then falls in the range $2.4 \lesssim \sigma \lesssim 3$ for the data reported in Figures 5 and 6. This still lies in the parameter space for superluminal shocks (Baring & Summerlin 2009), but requires somewhat stronger field turbulence than for the uncooled case, perhaps in the range $\delta B/B \lesssim 0.3$. Again Bohm-limited diffusion is not indicated. It is noted in passing that these claims are predicated on acceleration theory results generated for small angle scattering (i.e. pitch angle diffusion); if $\delta B/B \sim 1$ is considered, then one anticipates that larger angle deflections of charges will be active, resulting in much flatter spectra (e.g. Ellison, Jones & Reynolds 1990; Stecker, Baring & Summerlin 2007) that are incongruent with the Mrk 421 *Suzaku* data presented here. Such a large angle scattering regime may be more appropriate for the 2006 *Swift* observations of the intense flare in Mrk 421 (Tramacere et al. 2009), and for some flat spectrum gamma-ray sources in the *Fermi*-LAT database (Abdo et al. 2009).

For Mrk 421, 2009 observations by *Fermi*-LAT that are not contemporaneous with the *Suzaku* data presented here yield $\Gamma_\gamma \sim 1.78$ (Abdo et al. 2009). If this signal constitutes inverse Compton emission by uncooled electrons at Lorentz factors below γ_c ($< \gamma_{\max}$), then one infers $\sigma \sim 2.56$, not dissimilar from the *Suzaku* inference for strong cooling just above. Given that this GeV-band spectrum probably originates from electrons that emit synchrotron photons below the X-ray window, and that the steeper TeV spectrum ($\Gamma_\gamma \sim 2.91$ in the contemporaneous VERITAS data presented in Acciari et al. 2009) provides an approximate inverse Compton image of the X-ray synchrotron signal (with $\Gamma_2 \sim 2.5 - 2.9$ here), one expects the inferred σ for the *Fermi* data should be slightly lower than that for the *Suzaku* observations. Note also that historically, the radio spectrum for Mrk 421 is flatter still, at $\Gamma_{\text{rad}} \sim 1.1 - 1.3$ (e.g. see Makino, et al. 1987), suggesting $\sigma \sim 1.2 - 1.6$ for the electrons radiating at these frequencies. Taken together with the gamma-ray data, a picture emerges that the radiating lepton distribution might be injected with a “convex” distribution, i.e. with σ an increasing function of energy. Yet, care must be taken to explore the influence of non-cospatiality for the origin of the various emission components, and the role of synchrotron self-absorption, before diagnosing such a curvature in the injection distribution.

Let us delve deeper into a comparison between the cooled and uncooled emission scenarios. It is possible to envisage a cospatial competition between acceleration and synchrotron cooling, a paradigm that is commonly accepted in models of X-ray emission in Galactic supernova remnants (SNRs). While this can generate the observed variability in both flux and spectral index, unless diffusion in shock-layer turbulence is incredibly inefficient, the requirement that a cooling-limited synchrotron turnover fall in the *Suzaku* X-ray window constrains the shock speed u_1 to values around $0.01c$, independent of the strength of B , provided that the acceleration process is gyroresonant, which is the prevailing paradigm. This assertion can be justified using results from the discussion of cooling-limited SNR shock acceleration in Baring et al. (1999). Eq. (12) therein indicates that the acceleration rate gives $d\gamma_e/dt \propto (u_1/c)^2 eB/(\eta mc)$, where the ratio $\eta = \lambda/r_g \geq 1$ of the particle’s mean free path λ to its gyro-radius r_g measures the departure from isotropic Bohm diffusion ($\eta = 1$, i.e. $\delta B/B \sim 1$). This can be equated to the synchrotron loss rate $|d\gamma_e/dt| \propto \gamma_e^2 B^2$ in the comoving frame of the jet. The resulting electron Lorentz factor $\gamma_e \equiv \gamma_c \propto u_1(\eta B)^{-1/2}$ for cooling-limited acceleration can be inserted into the textbook formula for the characteristic synchrotron energy to yield a synchrotron peak/cutoff energy, that is independent of the field strength:

$$E_{\text{syn}} \sim \frac{\delta}{\eta} \left(\frac{u_1}{c} \right)^2 \frac{m_e c^2}{\alpha} \quad (1)$$

Here $\alpha = e^2/(\hbar c)$, and the blueshift due to Doppler beaming has been included. For $\delta = 1$, the $u_1 = c$, $\eta = 1$ limit of this is around 50 MeV, as was highlighted in De Jager et al. (1996) for considerations of gamma-ray emission at relativistic pulsar wind nebular shocks; see de Jager & Baring (1997) for a compact presentation of this critical energy.

To move E_{syn} into the classic X-ray band one has to set $u_1 \sim 0.01c$ if $\eta \gtrsim 1$ and lower still if $\delta > 1$. This lower shock speed is an attractive value for SNRs, but is clearly too small for blazar jet contexts. It is possible to adjust η to fix $u_1 \sim c$, which quickly leads to fitting values $\eta \sim 10^5$, thereby dramatically reducing the rapidity of the acceleration process. This was the approach of Inoue & Takahara (1996) when exploring

multiwavelength modeling of Mrk 421 spectra (they required even higher values $\eta \sim 10^7$ for their 3C 279 case study), who assumed $\delta \sim 10$. In the light of refined studies of acceleration at relativistic shocks, this is unsatisfactory on three counts. First, the parameter space of shocks that would generate indices σ that would accommodate the *Suzaku* indices is extremely constrained to the subluminal/superluminal boundary (e.g. see Baring 2010). Next, requiring $\eta > 10^4$ leads to extraordinarily inefficient injection of particles into the acceleration process (e.g. Baring & Summerlin 2009), imposing uncomfortable constraints on blazar energetics. Finally, such large values of η define essentially laminar fields that are not expected in shocks, which are inescapably turbulent. Hence, it is difficult to fine-tune a synchrotron-cooling limited-turnover in the X-ray band in the blazar model context.

In contrast, it is quite possible that a cooling break can be situated below the X-ray band, provided that the acceleration and cooling regions are spatially distinct. This is a preferred paradigm in many blazar models. Such a strongly-cooled case corresponds to static or impulsive acceleration at a shock, generating non-thermal electrons up to the maximum Lorentz factor (which can be $\gamma_e \gtrsim 10^6$ on timescales of a few seconds for $\eta \sim 1$ and $B \sim 0.1$ G), followed by escape from the shock environs and subsequent gradual cooling in a remote and more extended region that is defined by the competition between spatial diffusion/convection and radiative cooling. Flux and index variability driven by cooling effects would then tend to be muted by spatial and temporal convolutions. Moreover, spectral cooling breaks, if situated in the optical/UV band, would correspond to Lorentz factors $\gamma_e \sim 10^4 - 10^5$ and therefore yield cooling times of the order of days or longer. Hence the spectral variations on timescales of a few hours reported here very probably reflect intrinsic fluctuations in the acceleration/injection process, as opposed to spatial inhomogeneities such as magnetic field clumping in the cooling region. The spectral hysteresis evinced in Figures 5 and 6 possesses some similarities to, and significant differences from that envisaged in the competitive acceleration/cooling model of Kirk et al. (1998). *Flare 1* seems to suggest that alterations in shock conditions precipitate an increased injection rate \dot{n}_e (or an increased field) *before* flattening the distribution (lowering index σ), the system subsequently relaxing via reducing the injection rate or field strength and finally displaying signs of an incipient increase in σ . Field turbulence variations should drive injection and σ changes that contribute to both flux and hardness ratio alterations. *Flare 2* encapsulates another level of complexity, defying simple description.

To summarize, given these cooling/acceleration considerations, it seems likely that the variations depicted in Figures 5 and 6 signify changes in the lepton acceleration at the relativistic shocks contained in the Mrk 421 jet, perhaps with a smaller contribution from Doppler beaming fluctuations. The acceleration fluctuations are easily produced from a theoretical standpoint by just modest or small changes to the level of field turbulence, the mean field direction and amplitude, or the local density encountered in the shock environs as it traverses jet material. This claim is underpinned in part by the broad-ranging spectral index phase space plots presented in Baring & Summerlin (2009) and Baring (2010), together with their discussion of correlated injection efficiencies.

Finally, even though properties of the acceleration process may cause spectral variations in the X-ray band, we reiterate that most of the conclusions from earlier multiwavelength lep-

tonic modeling work are still valid (e.g. Krawczynski et al. 2001). A magnetic field of ~ 0.2 G is still needed so that electrons can emit a good fraction of their energy on ~ 1 hr time scales. Also, γ_{\max} and δ/B are still constrained by the relative peak positions of the SEDs in the x-ray and gamma-ray regimes. The inference of variations of the parameters of the acceleration process in jet shocks from observed X-ray SED fluctuations is a subtlety that does not substantially modify these more global parameters inferred from the broadband SED modeling, but does directly impact the relative apportionment of acceleration and cooling, in part through constraints imposed on $\eta = \lambda/r_g$.

5. SUMMARY

We present the results from a 4-day *Suzaku* observation of Mrk 421 while in a flaring state. The 0.5 keV - 30 keV flux decreased by a factor of 2 during the course of the observation. We find good agreement when fitting spectra from isolated time intervals with a galactic absorption + broken power-law model. Trends in the HR-flux plane indicate there are different timescales for competing processes which differ from flare to flare and for different flux levels. The X-ray spectral index changes by ~ 0.2 . However, the spectral evolution seems not to be related to the phase of a flare. The erratic relation between the light curves and the spectral indices suggests constraints on the interpretation of the shocked jet environment.

In the literature, the past observations have often been explained by invoking the competition of the acceleration and cooling time scales. However, it seems improbable that the timescales of acceleration and cooling are similar, since this would require jet shock speeds of the order of $0.01c$, and that the relative importance of shock acceleration and subsequent synchrotron cooling differs from flare to flare. We suggest here that it is more likely that the *Suzaku* data properties reported here are due to intrinsic changes in the acceleration process at relativistic shocks in the jet, producing electron distributions with varying spectral indices and changing maximum energies.

This research has made use of data obtained from the *Suzaku* satellite, a collaborative mission between the space agencies of Japan (JAXA) and the USA (NASA). AG and HK acknowledge support by the Suzaku Guest Investigator Programme, NASA grant NNX08AZ76G. MGB acknowledges support from National Science Foundation grant PHY07-58158 and NASA Astrophysics Theory grant NNX10AC79G. MGB is also grateful to the Kavli Institute for Theoretical Physics, University of California, Santa Barbara for hospitality during part of the period when this research was performed, a visit that was supported in part by the National Science Foundation under Grant No. PHY05-51164.

REFERENCES

- Abdo, A. A. et al. 2009, *ApJ*, 707, 1310.
 Abdo, A. A. et al. 2010a, *Nature*, 463, 919.
 Abdo, A. A. et al. 2010b, *ApJ*, in press. [[astro-ph/1004.0348](#)]
 Acciari, V. A., Aliu, E., Aune, T., et al. 2009, *ApJ*, 703, 169.
 Acciari, V. A., Aliu, E., Aune, T., et al. 2010, *ApJ*, submitted.
 Aharonian, F. A. 2000, *New Astronomy*, 5, 377.
 Aharonian, F. A. et al. 2002, *A&A*, 393, 89.
 Baring, M. G. 2010, *Adv. Space Res.*, in press. [[astro-ph/1002.3848](#)]
 Baring, M. G. et al. 1999, *ApJ*, 513, 31.
 Baring, M. G. & Summerlin, E. J. 2009, in “Shock Waves in Space and Astrophysical Environments,” eds. X. Ao, R. Burrows & G. P. Zank (AIP Conf. Proc., 1183, New York) p. 74. [[astro-ph/0910.1072](#)]
 Bednarek, W. & Protheroe, R. J. 1997, *MNRAS*, 292, 646.
 Blazejowski, M. et al. 2005, *ApJ*, 630, 130.
 Böttcher, M. et al. 1997, *A&A*, 324, 395.
 Cui, W. 2004, *ApJ*, 605, 662.
 De Jager, O. C. et al. 1996, *ApJ*, 457, 253.
 De Jager, O. C. & Baring, M. G. 1997, *AIP Conf. Proc.*, 410, 171.
 Ellison, D. C. & Double, G. P. 2004, *Astropart Phys.*, 22, 323.
 Ellison, D. C., Jones, F. C. & Reynolds, S. P. 1990, *ApJ*, 360, 702.
 Fossati, G. et al. 2000, *ApJ*, 541, 166.
 Fossati, G. et al. 2008, *ApJ*, 677, 906.
 Georganopoulos, M. & Kazanas, D. 2004, *ApJL*, 604, L81.
 Ghisellini, G. & Maraschi, L. 1989, *ApJ*, 340, 181.
 Ghisellini, G., Tavecchio, F., & Chiaberge, M. 2005, *A&A*, 432, 401.
 Giannios, D., Uzdensky, D. A., & Begelman, M.C. 2009, *MNRAS*, 395, L29.
 Gruber, D. E. et al. 1999, *ApJ*, 520, 124.
 Gupta, A. C., Acharya, B. S., Bose, D., Chitnis, V. R., & Fan, J. 2008, *ChJAA*, 8, 395.
 Homan, D. C., Roopeshi, O., Wardle, J. C., & Roberts, D. H. 2001, *ApJ*, 549, 2.
 Inoue, S. & Takahara, F. 1996, *ApJ*, 463, 555.
 Ishisaki, Y. et al. 2007, *PASJ*, 59, S113.
 Jokipii, J. R. 1987, *ApJ*, 313, 842.
 Kardeshev, N. S. 1962, *Soviet Astronomy*, 6, 317.
 Kataoka, J., Takahashi, T., Makino, F. et al. 2000, *ApJ*, 528, 243.
 Kirk, J. G. & Heavens, A. F. 1989, *MNRAS*, 239, 995.
 Kirk, J. G. & Schneider, P. 1987, *ApJ*, 315, 425.
 Kirk, J. G., Rieger, F. M. & Mastichiadis, A. 1998, *A&A*, 333, 452.
 Kokubun, M. et al. 2007, *PASJ*, 59, S53.
 Koyama, K. et al. 2007, *PASJ*, 59, 23.
 Krawczynski, H., Sambruna, R., Kohnle A. et al. 2001, *ApJ*, 559, 187.
 Krawczynski, H. et al. 2004 *ApJ*, 601, 151.
 Krennick et al. 2002, *ApJL*, 575, L9.
 Lister, M.L. & Smith, P.S. 2000 *ApJ*, 541, 1.
 Lyutikov, M. 2003, *New Astr. Rev.*, 47, 513.
 Macomb, D. J. et al. 1995, *ApJL*, 449, L99.
 Makino, F., Tanaka, Y., Matsuoka, M., et al. 1987, *ApJ*, 313, 662.
 Mannheim, K. 1993, *A&A*, 269, 67.
 Massaro, E., Perri, M., Giommi, P., Nesci, R., & Verrecchia, F. 2004, *A&A*, 422, 103.
 Mastichiadis, A. & Kirk, J. G. 1997, *A&A*, 320, 19.
 Mitsuda, K. et al. 2007, *PASJ*, 59, S9.
 Mücke, A., Protheroe, R. J., Engel, R., Rachen, J. P., & Stanev, T. 2003, *Astroparticle Physics*, 18, 593.
 Padovani, P. & Giommi, P. 1995, *MNRAS*, 277, 1477.
 Piner, B. G. & Edwards, P. G. 2005, *ApJ*, 622, 2.
 Punch, M. et al. 1992, *Nature*, 358, 477.
 Rebillot, P. F. et al. 2006 *ApJ*, 641, 740.
 Rees, M. J. 1978, *MNRAS*, 184, P6.
 Sato, R., Kataoka, J., Takahashi, T., Madjeski, G. M., Rugamer, S., & Wagner, S. J. 2008, *ApJ*, 680, L9.
 Spada, M. et al. 2001, *MNRAS*, 325, 1559.
 Stawarz, L. & Petrosian, V. 2008, *ApJ*, 681, 2.
 Stecker, F. W., Baring, M. G. & Summerlin, E. J. 2007, *ApJL*, 667, L29.
 Takahashi, T. et al. 1996, *ApJL*, 470, L89.
 Takahashi, T. et al. 2000, *ApJL*, 542, L105.
 Takahashi, T. et al. 2007, *PASJ*, 59, S35.
 Tanihata, C. et al. 2001, *ApJ*, 563, 569.
 Tramacere, A., Massaro, F., & Cavaliere, A. 2007, *A&A*, 466, 521.
 Tramacere, A., Giommi, P., Perri, M., Verrecchia, F., & Tosti, G. 2009, *A&A*, 501, 3.
 Ushio, M., et al. 2009, *ApJ*, 699, 1964.